communications earth & environment

A Nature Portfolio journal

Article

https://doi.org/10.1038/s43247-026-03194-8

Salt fingers contribute substantially to diapycnal oxygen transport into the oxygen minimum zone of the eastern South Pacific

Mauro Pinto-Juica[1,2] ✉, Oscar Pizarro[1,3] ✉, Ángel Rodríguez-Santana[4], Luis P. Valencia[5], Osvaldo Ulloa[1,6], Pedro A. Figueroa[7], Marcel Ramos[8] & Bastien Y. Queste[2]

Oxygen minimum zones are large-scale subsurface oxygen-deficient layers experiencing rapid reconfiguration under climate change, partly driven by changes in ventilation whose mechanisms remain poorly understood. Along the eastern South Pacific oxygen minimum zone, a subsurface salinity maximum associated with equatorial subsurface water creates thermohaline gradients that trigger salt-finger instabilities across the lower oxycline. Here we show, using high-resolution microstructure, velocity, and oxygen observations, that these instabilities enhance diapycnal mixing and drive significant oxygen fluxes into the oxygen-deficient layer. While the upper oxycline is dominated by shear-driven turbulence, strong stratification suppresses vertical mixing, resulting in low diffusivities where sharp oxygen gradients are present, whereas salt fingering below yields high diffusivities where gradients are weaker, leading to comparable oxygen fluxes across both boundaries. The widespread occurrence of salt-finger-favorable conditions across the eastern South Pacific suggests that this mechanism plays a persistent and previously unrecognized role in the oxygen minimum zone ventilation.

Oxygen minimum zones (OMZs) are large-scale subsurface layers in the ocean where oxygen concentrations fall to extremely low levels, typically forming in subtropical and tropical eastern boundary systems where sluggish circulation leads to weak ventilation, creating "shadow zones"[1–4]. These poorly ventilated regions often co-occur with the productive surface waters of eastern boundary upwelling systems, where high primary production and the subsequent remineralization of sinking organic matter drive intense oxygen demand in the OMZ[5,6].

In the current context of climate change, there is growing concern about the rapid decline of oxygen levels in the global ocean[7,8]. Understanding the drivers of this deoxygenation, as well as the potential spatial reconfiguration of OMZs that may result, is therefore critical[9,10]. OMZs act as respiratory barriers for many pelagic species[4,11,12] and alter biogeochemical cycles by promoting anaerobic pathways, such as denitrification and anammox[13–15]. Consequently, quantifying the processes that regulate oxygen exchange across OMZ boundaries is essential for constraining regional oxygen budgets and for projecting the future evolution of OMZs under ongoing climate change[10,16].

Diapycnal mixing, spanning scales from meters to millimeters[17], is mainly driven by vertical shear, internal-wave breaking, and double-diffusive processes[18]. Internal-wave-driven mixing varies with stratification, topography, and wind forcing[19], whereas double diffusion arises from the unequal molecular diffusivities of heat and salt. When a warm, salty layer overlies a cooler, fresher one, a common configuration in subtropical oceans, the faster diffusion of heat allows parcels to lose buoyancy more quickly than they lose salt, producing narrow downward-moving plumes known as salt fingers. These small-scale structures efficiently transfer heat, salt, and dissolved substances vertically, substantially increasing local

---

[1]Millennium Institute of Oceanography, Universidad de Concepción, Concepción, Chile. [2]Department of Marine Science, University of Gothenburg, Gothenburg, Sweden. [3]Departamento de Geofísica, Universidad de Concepción, Concepción, Chile. [4]ECOAQUA, Universidad de Las Palmas de Gran Canaria, Las Palmas de Gran Canaria, España. [5]University Institute for Research in Sustainable Aquaculture and Marine Ecosystems, Las Palmas de Gran Canaria, España. [6]Departamento de Oceanografía, Universidad de Concepción, Concepción, Chile. [7]Department of Earth and Environment, Boston University, Boston, MA, USA. [8]Departamento de Biología Marina, Facultad de Ciencias del Mar, Universidad Católica del Norte, Coquimbo, Chile. ✉e-mail: mauro.pinto.j@gu.se; opizarro@udec.cl

diffusivities[20–22]. Both shear-driven and double-diffusive mixing contribute to OMZs ventilation. Font et al.[23] evaluated the potential for both processes using hydrographic stability diagnostics, highlighting the widespread occurrence of conditions favorable to double diffusion. Complementing this, Fischer et al.[24] showed that double diffusion can enhance turbulent diffusivity by up to ~50% below the OMZ core, underscoring its importance for vertical exchange.

One of the most extensive and well-defined OMZs globally is associated with the Peru–Chile upwelling system, which forms the southern extent of the eastern South Pacific OMZ (ESP-OMZ). Beneath the productive surface layer, oxygen concentrations decrease rapidly to hypoxic ($< 60\,\mu\text{mol}\,\text{L}^{-1}$) or even functionally anoxic levels ($< 10\,\text{nmol}\,\text{L}^{-1}$; below the detection limit of current sensors)[25–27]. Low-oxygen waters in this region extend from the equator to approximately 40°S, reaching as far as 180 km offshore at 36.5°S. The vertical structure of the ESP-OMZ is bounded by two contrasting interfaces: a sharp upper oxycline, between 100 and 150 m depth, separating well-oxygenated surface waters from the OMZ, and a more gradual lower oxycline, generally found between 250 and 450 m, marking the transition to oxygen-rich intermediate waters[5,28]. These gradients arise from the interplay between isopycnal and diapycnal transport, which together regulate the oxygen content and biogeochemistry of the OMZ[3].

Off central Chile (~36.5°S), the ESP-OMZ coincides with the equatorial subsurface water (ESSW), a water mass characterized by a subsurface salinity maximum[29,30]. The ESSW is transported southward by the Peru–Chile undercurrent, which carries low-oxygen, high-salinity waters from the eastern tropical Pacific along the continental slope to latitudes beyond 40°S[28,31,32]. The ESP-OMZ is flanked by two fresher, well-ventilated water masses: the shallow salinity minimum water (SSMW; also known as eastern South Pacific intermediate water) above, and the Antarctic Intermediate Water (AAIW) below[29,30,33]. Interactions among these water masses create strong thermohaline gradients at the OMZ boundaries, where contrasting temperature–salinity properties favor double-diffusive instability. Although salt-finger-driven mixing has been suggested in this region[29], its role, particularly across the ESSW–AAIW transition, remains poorly quantified. At the lower boundary of the ESP-OMZ, the strong thermohaline contrasts promote double-diffusive instabilities that enhance diapycnal transport of oxygen-rich waters from the AAIW into the oxygen-depleted ESP-OMZ core. This vertical mixing could be critical in sustaining or modulating the structure and ventilation of the ESP-OMZ, yet it has not been quantitatively assessed.

While recent studies have emphasized the role of mesoscale-driven isopycnal fluxes such as eddies, filaments, and frontal intrusions in ventilating the OMZs[23,32,34–37], the contribution of diapycnal mixing—especially that driven by double diffusion— remains poorly constrained, particularly within the ocean interior and near the lower oxycline. Given the pronounced thermohaline contrasts in this region, double-diffusive processes may constitute a significant and persistent pathway for oxygen supply to the ESP-OMZ. Understanding this pathway is essential for accurately anticipating the response of the ESP-OMZ to the ongoing ocean deoxygenation.

In this study, we provide quantitative estimates of diapycnal mixing driven by salt-finger instabilities at the southern boundary of the ESP-OMZ, off central Chile. Combining microstructure measurements, CTD-O casts, and ADCP observations from the continental slope off central Chile near 36.5°S, we investigate how thermohaline gradients across the lower oxycline contribute to enhanced vertical mixing. We specifically highlight that the salt-finger driven diffusivity at the lower oxycline, despite weaker oxygen gradients, results in diapycnal oxygen fluxes comparable to those induced by shear-driven mixing across the sharper upper oxycline.

Results

Background conditions

All observations were conducted over the upper slope (~75 km offshore, over the 600 m isobath; Fig. 1a–c). Surveys were timed during relatively mild wind periods (Fig. 2; See also Supplementary Note 1) to ensure safe operations aboard the R/V Kay-Kay-II (~18.5 m length). This site was selected because the lowest dissolved oxygen (DO) concentrations at this latitude are typically found along the shelf break and upper slope. Additionally, the transition from the OMZ to the core of the low-salinity, well-ventilated AAIW is clearly identifiable at this location (Figs. 3c and S1a–c).

In January 2020, measurements were conducted at three stations spanning the transition from the slope to the continental shelf (Fig. 1a) to assess spatial variability. In contrast, the July 2021 (Fig. 1b) and October 2022 (Fig. 1c) surveys focused on repeated measurements at approximately the same site. Multiple microstructure and CTD profiles were collected at each station during all campaigns (Tables S1 and S2). The January 2020 campaign followed a strong upwelling event, although wind conditions had relaxed by the time of sampling. In contrast, July 2021 measurements were made under mild downwelling conditions, while October 2022 sampling occurred during relatively calm periods (Fig. 2).

Across all surveys, the observed water-mass structure was consistent with regional hydrography[38]. $\Theta - S_A$ diagrams (Fig. 4a–c) reveal a strong salinity contrast between the SSMW, ESSW, and AAIW within the upper 600 m. Although general water-mass structure patterns remained stable, notable differences between campaigns were observed: for instance, the

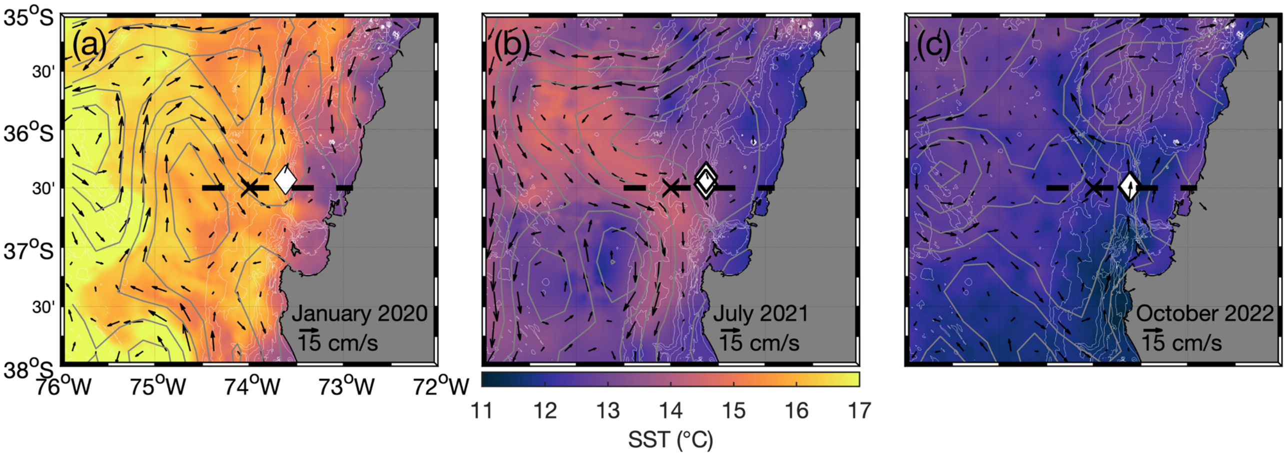

Fig. 1 | Surface hydrographic context during the observation periods. Sea surface temperature (colors, in °C), satellite-derived sea surface height anomalies (gray contours), and associated surface geostrophic velocity anomalies (arrows) during the three measurement periods: **a** January 2020, **b** July 2021, and **c** October 2022. Thin white contours denote bathymetric isobaths. Diamonds mark the locations of microstructure and CTD-O profile stations. The dashed line indicates the glider transect shown in Fig. 3d, and X symbols correspond to the locations used for the $\Theta - S_A$ diagram in Fig. 3c.

salinity maximum (and associated DO minimum) was more pronounced in January 2020 compared to October 2022. These variations likely reflect seasonal or intraseasonal fluctuations that modulate the depth, intensity, and extent of the OMZ[35], likely driven by changes in the intensity of the Peru–Chile undercurrent or by intra-thermocline eddy activity that transports low-oxygen waters from the continental shelf offshore.

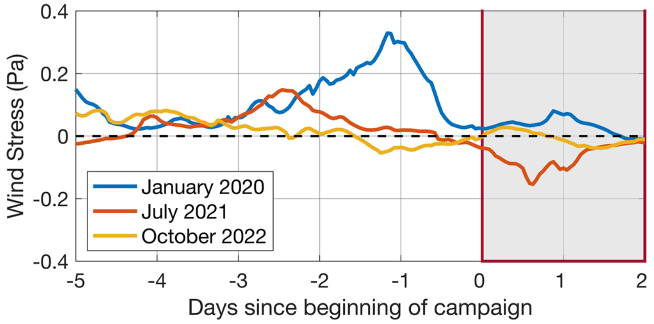

Fig. 2 | Alongshore wind stress preceding each field campaign. Alongshore wind stress calculated over the 5 days preceding each field campaign: January 2020 (blue), July 2021 (orange), and October 2022 (yellow). The red box indicates the period during which field measurements were conducted.

Salinity variations along isopycnal surfaces further highlight the presence of SSMW and AAIW intrusions into the OMZ, especially between isopycnals 26.3 and 26.55 kg m^{-3} (Fig. 4). These intrusions are often marked by localized increases in DO and decreases in salinity and are associated with vertical thermal inversions observed in CTD-O profiles (Supplementary Fig. S1). Such features suggest the presence of fine-scale interleaving layers or intrusions likely generated by submesoscale processes, including intra-thermocline eddies and shear-driven lateral stirring[39]. These mechanisms can distort the background stratification and generate strong vertical and lateral thermohaline gradients, thereby creating favorable conditions for double-diffusive instabilities. In particular, the resulting perturbations to the local temperature–salinity structure can promote salt-fingering, as reflected in the Turner angle distributions described in the following section.

Double diffusive conditions in the ESP-OMZ

To illustrate conditions favorable for double-diffusive instabilities, we estimated the Turner angle (Tu) along the western coast of South America (Fig. 3b, see also supplementary Note 2). A subsurface salinity maximum, corresponding to the core of the ESSW and the OMZ, is present throughout the section. Beneath this maximum, the lower oxycline marks the transition from the warm, saline, oxygen-depleted ESSW to the colder, fresher, and more oxygenated AAIW. Favorable conditions for salt-finger formation,

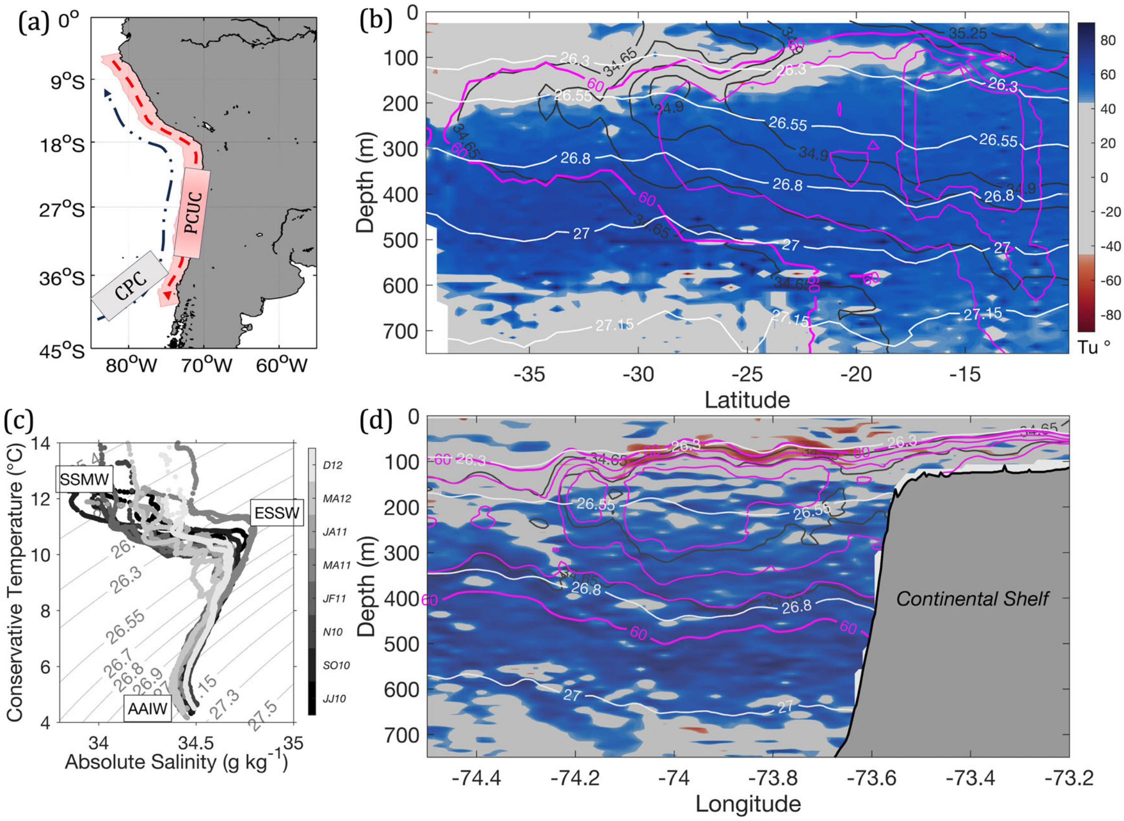

Fig. 3 | Regional circulation, water-mass structure, and double-diffusive context of the eastern South Pacific OMZ. a Schematic of the main currents in the eastern South Pacific, including the surface Chile–Peru current (CPC) and the subsurface Peru–Chile undercurrent (PCUC). **b** Mean characteristics of the oxygen minimum zone (OMZ) along the Peruvian and Chilean coasts, based on historical CTD profiles (1980–2022) from the world ocean database (WOD) within the red-shaded region shown in Fig. 3a. Turner angles (Tu, in colors) indicate double-diffusive instability; conditions favorable for salt-finger ($Tu > 45°$) are commonly observed below the OMZ core (magenta contours, in µmol L^{-1}). Absolute salinity (black contours, in g kg^{-1}) and potential density anomaly σ_t (white contours, in kg m^{-3}) are also shown. Note the alignment of maximum salinities with minimum oxygen concentrations. **c** Temperature–salinity ($\Theta-S_A$) diagram of a CTD station at approximately 36.5°S, 74°W, sampled during eight surveys conducted in different seasons between 2010 and 2012. Gray scales indicate the month and year of each transect. Water masses identified include the shallow salinity minimum water (SSMW), equatorial subsurface water (ESSW), and Antarctic intermediate water (AAIW). The transition between ESSW and AAIW coincides with high Turner angles shown in (**b**, **d**). **d** Offshore glider section conducted from 1 April to 12 April 2011 along 36.5°S, spanning from ~73°W (coast) to 74.5°W, illustrating fine-scale thermohaline features. Additional glider sections are available in the Supplementary Material (Note 3 and Fig. S4).

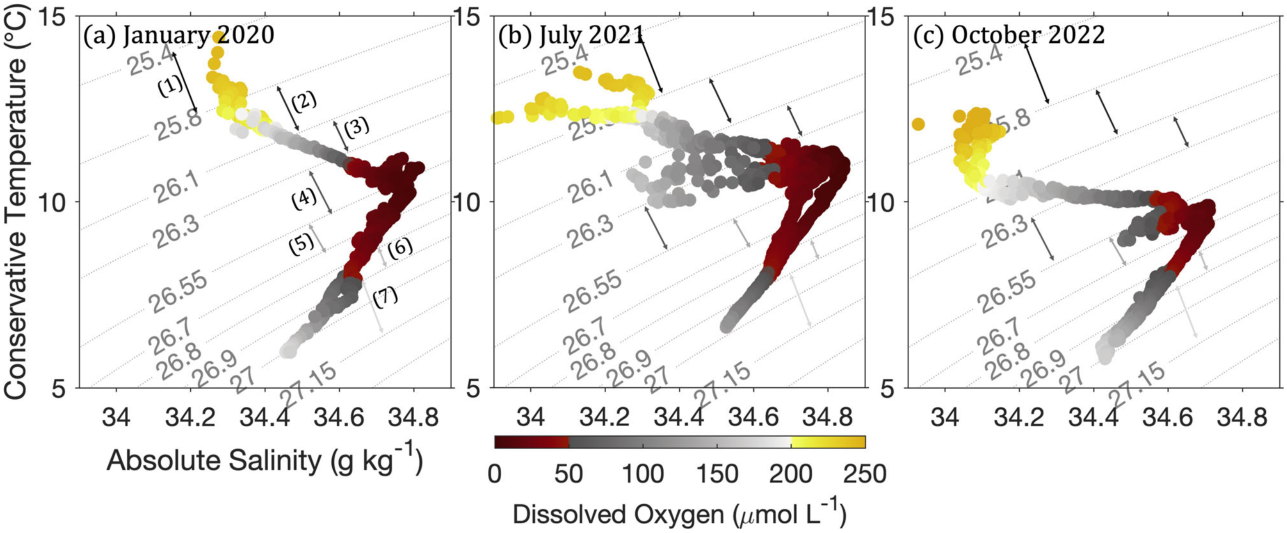

Fig. 4 | Thermohaline structure and water-mass distribution during the three observation periods. Conservative temperature–absolute salinity ($\Theta - S_A$) diagrams based on CTD-O profiles for **a** January 2020, **b** July 2021, and **c** October 2022. Colors represent dissolved oxygen concentrations (in µmol L^{-1}). Arrows indicate the potential density anomaly (σ_t) intervals used to calculate net diapycnal diffusivity. The $\Theta - S_A$ structure reflects the influence of three dominant water masses within the upper ~600 m: the SSMW (surface to 26.3 kg m^{-3}), the ESSW (26.3–26.8 kg m^{-3}), characterized by a salinity maximum, and the underlying AAIW (26.8 kg m^{-3} to the bottom), which is well-ventilated and low in salinity. These σ_t ranges were defined from all historical profiles shown in Fig. 3c.

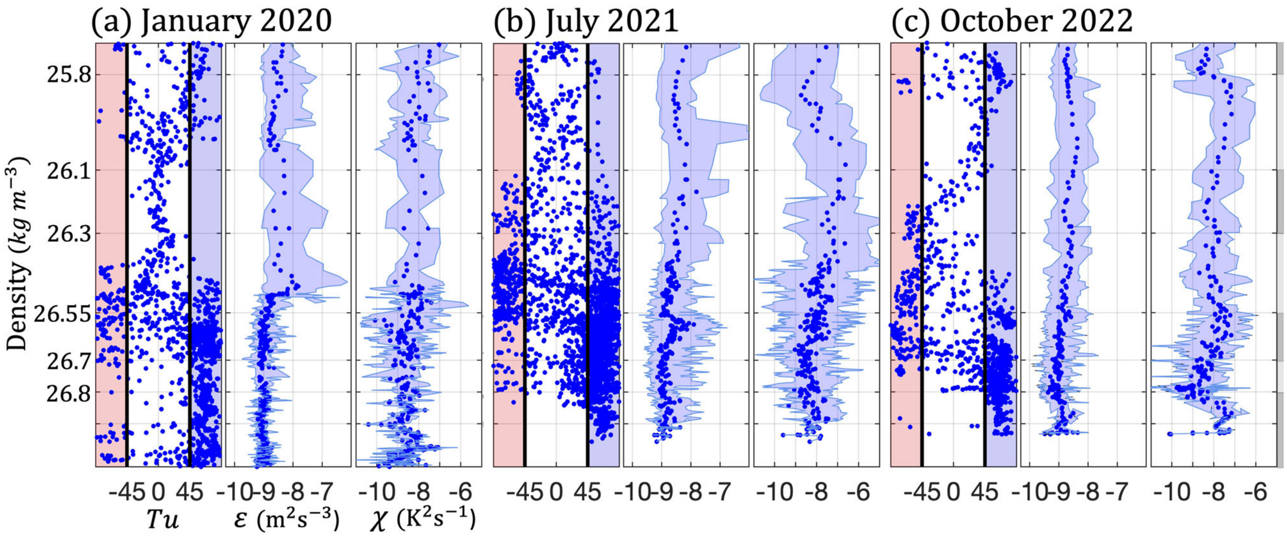

Fig. 5 | Turner angle and microstructure-derived dissipation rates across density space. a–c show: Turner angle (Tu, °), log$_{10}$ turbulent kinetic energy dissipation rate (ε, m^2 s^{-3}), and log$_{10}$ thermal variance dissipation rate (χ, K^2 s^{-1}) profiles based on the VMP casts as a function of potential density anomaly for the three campaigns. The Tu profiles show all computed values as blue dots, blue and red shading corresponds to conditions favorable for salt fingers and convective double diffusion, respectively. Blue dots represent the median ε and χ values calculated across all profiles at each measurement depth. These medians are plotted against the corresponding median potential density. The shading indicates the range between the minimum and maximum values of each respective campaign. Gray bars on the right indicate each density interval, see Table 1 (column 3) for the mean depth of each interval.

defined as $Tu > 45°$ (indicated by dark blue in Fig. 3b, d), are evident within this transitional layer. North of ~30°S, $Tu > 45°$ values also appear near the surface, where warm, saline subtropical waters overlie a shallow salinity minimum[29,30].

Given that merging and assemblage of historical hydrographic datasets may smooth vertical gradients and obscure mesoscale or fine-scale features, we complemented this analysis with Turner angles estimated from a glider section conducted along 36.5°S (Fig. 3d, see also supplementary Note 3). The glider observations confirm favorable conditions for salt fingering within the ESSW–AAIW transition zone (Fig. 3c, d) and are further detailed in Supplementary Fig. S4a–c. In contrast to the smoothed historical data, the glider section reveals pronounced fine-scale structures, likely the result of small-scale intrusions of surface water into the ESP-OMZ, driven by mesoscale stirring[40] and/or interleaving processes[41–43].

Turbulence characteristics near the core of the ESP-OMZ

During January 2020, July 2021, and October 2022, salinity maxima consistently aligned with the 26.55 kg m^{-3} isopycnal, also marking the core of the OMZ (Fig. 4a–c). Beneath these maxima, Tu values remained above 45° across all three periods (Fig. 5a–c), indicating persistent conditions favorable for salt-finger instabilities. Median values of the dissipation rates of turbulent kinetic energy (ε) ranged from 10^{-9} to 10^{-8} m^2 s^{-3}, while thermal variance dissipation rates (χ) ranged from 10^{-10} to 10^{-7} K^2 s^{-1}. Both ε and χ exhibited a slight decrease below the 26.55 kg m^{-3} isopycnal, reflecting

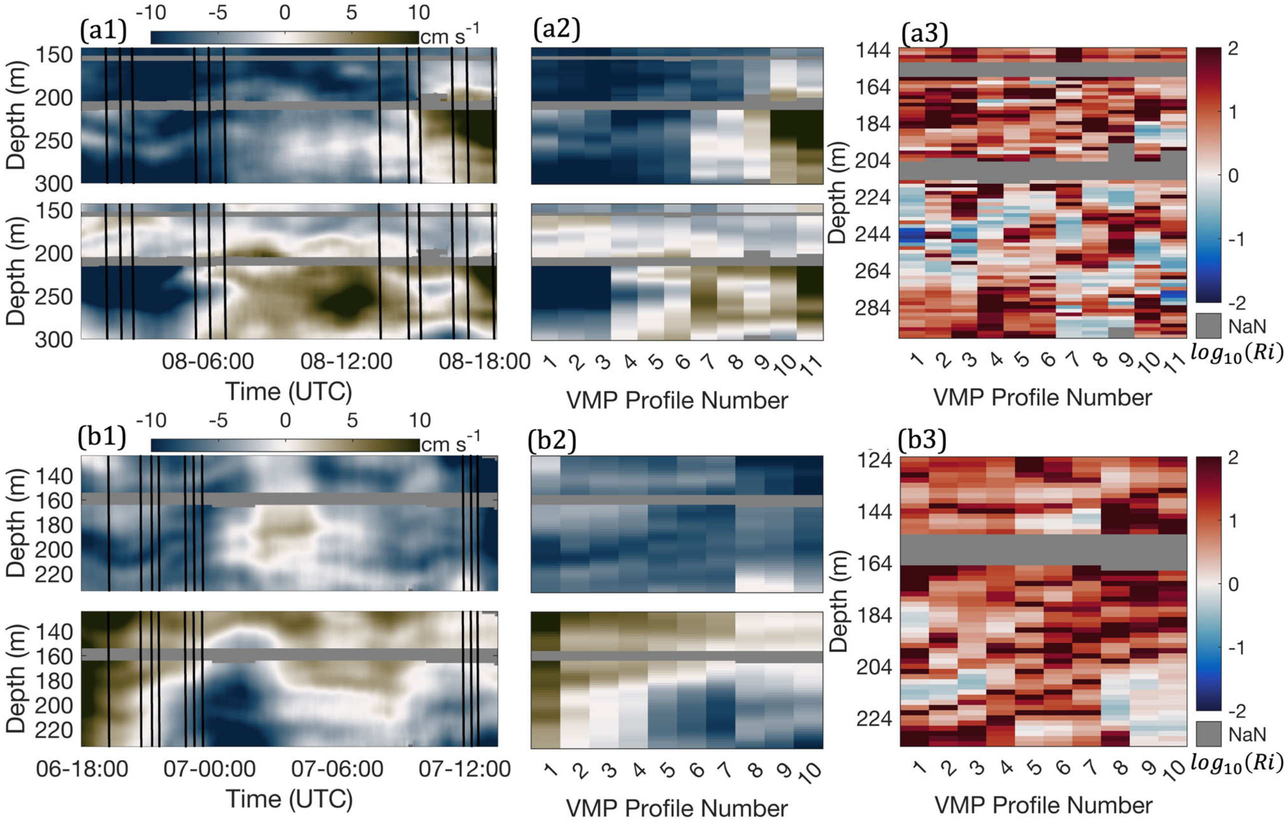

Fig. 6 | Velocity shear and gradient Richardson number during the 2021 and 2022 campaigns. Time series of horizontal velocity and corresponding profiles of the gradient Richardson number (Ri, $\log_{10}$ scale) during **a** July 2021 and **b** October 2022. To synchronize the ADCP data with the VMP profiles, horizontal current measurements of July 2021 were averaged over 2-min intervals. Then, a 31-point moving mean was applied in the time domain to filter out high-frequency variability, followed by a 10 m moving average in the vertical. A representative current profile was then computed by averaging over the duration of each VMP-250 fall (typically 10–15 min). (a1, b1) Time-averaged eastward (upper) and northward (lower) velocity components measured by ADCP array. Vertical black lines indicate the timing of VMP profiles. (a2, b2) eastward (upper) and northward (lower) velocity profiles selected from the duration of the VMP-250 descent. These profiles were used to compute the vertical shear along with N^2 to estimate Ri. (a3, b3) Ri profiles computed by combining vertical shear from ADCP data with stratification derived from co-located VMP-CTD casts, using 2 m vertical bins. Only the depth ranges where ADCP data were available are shown. Gray shading denotes regions where Ri could not be computed due to the array gaps. See Supplementary Note 5 for further details on methodology.

reduced turbulence with depth. The median values of ε and χ obtained from microstructure profiles (indicated by blue dots in Fig. 5) are consistent with those typically reported in quiescent thermocline regions[18,44–46].

Gradient Richardson numbers (Ri), calculated from combined ADCP and VMP-CTD profiles collected in July 2021 and October 2022 (Fig. 6), exceeded unity in 80% and 91% of the observations, respectively. These measurements were obtained within a localized sector near the core of the OMZ, where ADCP velocity data were available, spanning approximately the 150–300 m depth range. In this stratified layer, $Ri > 1$ and density ratio values ($1 < R_\rho < 2$) indicate conditions favorable for active salt fingering[20,21] (see also Supplementary Note 5). However, intermittent episodes of Ri <1 were also detected during both campaigns, pointing to the occurrence of shear instabilities[47], particularly within sharp velocity gradients resolved near the lower oxycline. Although Ri is unavailable below ~300 m, the density-ratio criterion defining salt-finger-favorable conditions can be evaluated throughout the profile and provides a good, complementary discrimination of double-diffusive regimes, generally more direct than Ri for this purpose[21].

Diffusivities and diapycnal oxygen fluxes

Microstructure measurements were used to compute diffusivities and diapycnal oxygen fluxes across 7 selected potential density intervals (σ_t, indicated by arrows in the $\Theta - S_A$ diagrams, Fig. 4; density ranges provided in Table 1, columns 1–2). For each interval, mean depths, average density ratios ($\bar{R}_\rho$), and mean squared buoyancy frequencies ($\bar{N}^2$) are summarized in Table 1, along with their corresponding standard deviations. Ensemble averaged turbulent kinetic energy dissipation rates ($\langle\varepsilon\rangle$) and thermal variance dissipation rates ($\langle\chi\rangle$), derived from the microstructure data, were combined with these parameters to calculate two diffusivity components within each σ_t interval: K_{st}, representing shear-driven turbulent mixing, and K_{sf}, representing mixing due to salt-finger instabilities. The latter was estimated exclusively in regions where salt fingering is expected to be active ($1 < R_\rho < 2$, $Ri > 1$; see Methods and Supplementary Note 5 for details).

Near the core of the OMZ and just below the salinity maximum associated with ESSW, K_{sf} exceeded K_{st} by one to two orders of magnitude (Table 2), indicating that salt fingering is the dominant mechanism of diapycnal mixing at the lower oxycline adjacent to the OMZ. Net diapycnal diffusivity K, was calculated following the methodology of St. Laurent and Schmitt[21], by weighting K_{st} and K_{sf} according to their respective occurrence fractions (P_t, P_f). This net diffusivity, combined with vertical oxygen gradients derived from CTD-O profiles, was used to estimate diapycnal DO fluxes and their vertical divergences across density layers (Table 2, columns viii–ix). Within the OMZ layers (density intervals 2–7), oxygen flux divergences ranged from $-0.27\,\mu\text{mol}\,\text{L}^{-1}\,\text{day}^{-1}$ to $0.53\,\mu\text{mol}\,\text{L}^{-1}\,\text{day}^{-1}$ with predominantly negative values indicating a net convergence, i.e., accumulation of DO within these layers.

To assess the relative contribution of ventilation from the upper versus lower boundaries, we compared average diapycnal oxygen fluxes across density intervals (2)–(4) for January and July, and (2)–(5) for October (upper oxycline), and intervals (5)–(7) for January and July, and (6)–(7) for

Table 1 | Physical properties within potential-density anomaly intervals used for diffusivity and flux calculations

$N_\circ$	ρ (kg m^{-3})	$\lvert\bar{z}\rvert$ (m)	$\bar{N}^2 \times 10^{-5}$ (s^{-2})	$\bar{\Theta}_z$ (K m^{-1})	$\bar{R}_\rho$	$\langle\chi\rangle \times 10^{-8}$ (K^2 s^{-1})	$\langle\varepsilon\rangle \times 10^{-8}$ (m^2 s^{-3})
January 2020							
(1)	< -25.8[	36 ± 10	9.30 ± 0.54	0.044 ± 0.0029	−14 ± 3.75		0.7 ± 0.18
(2)	]25.80-26.10]	69 ± 18	5.07 ± 0.12	0.018 ± 0.0004	−1.8 ± 0.08		0.7 ± 0.12
(3)	]26.10-26.30]	92 ± 16	11.05 ± 0.54	0.029 ± 0.0013	−0.9 ± 0.06		2.9 ± 1.25
(4)	]26.30-26.55]	137 ± 27	2.71 ± 0.07	0.008 ± 0.0003	−0.9 ± 0.06		0.9 ± 0.13
(5)	]26.55-26.70]	246 ± 47	0.72 ± 0.01	0.006 ± 0.0001	3.9 ± 0.18	4.66 ± 2.59	0.1 ± 0.01
(6)	]26.70-26.80]	329 ± 19	1.51 ± 0.02	0.015 ± 0.0002	3.3 ± 0.15	0.63 ± 0.14	0.1 ± 0.01
(7)	]26.80->]	481 ± 70	0.90 ± 0.01	0.012 ± 0.0001	2.5 ± 0.04	3.13 ± 1.12	0.1 ± 0.01
July 2021							
(1)	< -25.8[	35 ± 10	5.90 ± 0.38	0.017 ± 0.0008	−1.1 ± 0.13		1.7 ± 0.57
(2)	]25.80-26.10]	47 ± 11	10.69 ± 0.25	0.025 ± 0.0012	−0.7 ± 0.04		1.3 ± 0.35
(3)	]26.10-26.30]	72 ± 11	6.82 ± 0.14	0.021 ± 0.0018	−1.2 ± 0.15		2.7 ± 1.2
(4)	]26.30-26.55]	145 ± 37	1.50 ± 0.02	0.003 ± 0.0002	−0.6 ± 0.05		0.4 ± 0.03
(5)	]26.55-26.70]	279 ± 44	0.91 ± 0.01	0.007 ± 0.0001	5.3 ± 0.14	6.19 ± 1.72	0.8 ± 0.05
(6)	]26.70-26.80]	393 ± 25	1.19 ± 0.01	0.011 ± 0.0001	3.6 ± 0.11	3.89 ± 1.97	0.2 ± 0.02
(7)	]26.80->]	470 ± 26	1.65 ± 0.02	0.018 ± 0.0002	3.3 ± 0.09	3.15 ± 0.86	0.3 ± 0.03
October 2022							
(1)	< -25.8[	33 ± 6	6.05 ± 0.36	0.020 ± 0.0011	−1.5 ± 0.33		0.2 ± 0.01
(2)	]25.80-26.10]	58 ± 9	9.46 ± 0.27	0.048 ± 0.0015	−7.3 ± 0.61		0.4 ± 0.03
(3)	]26.10-26.30]	84 ± 7	8.35 ± 0.19	0.012 ± 0.0013	−0.3 ± 0.03		0.3 ± 0.03
(4)	]26.30-26.55]	123 ± 18	4.08 ± 0.06	0.004 ± 0.0002	−0.2 ± 0.01		0.3 ± 0.01
(5)	]26.55-26.70]	192 ± 26	1.74 ± 0.02	0.003 ± 0.0003	−0.4 ± 0.04		0.2 ± 0.01
(6)	]26.70-26.80]	280 ± 30	0.90 ± 0.01	0.008 ± 0.0001	4.2 ± 0.13	2.38 ± 1.23	0.2 ± 0.12
(7)	]26.80->]	362 ± 23	2.00 ± 0.04	0.025 ± 0.0005	2.5 ± 0.07	2.02 ± 0.33	0.2 ± 0.01

Columns: (i) potential density-anomaly interval; (ii) mean depth corresponding to each interval (±one standard deviation); (iii) mean buoyancy frequency squared; (iv) mean vertical temperature gradient; (v) mean density ratio (from interval-mean $\bar{\Theta}_z$ and $\bar{S}_z$); (vi) ensemble average thermal-variance dissipation rate (restricted to samples meeting the salt-finger criterion); and (vii) ensemble average turbulent kinetic energy dissipation rate. For (iii)–(v), values are interval means estimated from degree−1 least-squares fits, and the "±" denotes the standard error of the fit. For (vi)–(vii), values are ensemble means over independent, non-overlapping 2-m segments; uncertainty is the bootstrap standard error (standard deviation of the bootstrap distribution of the mean) computed from 8 M resamples per interval (following St. Laurent and Schmitt[21]), where M is the number of independent segments.

October (lower oxycline). Mean oxygen fluxes across the upper oxycline were –7.26, –7.9, and –1.33 µmol L^{-1} m day^{-1} for January 2020, July 2021, and October 2022, respectively. At the lower boundary, mean fluxes were 5.60, 3.59, and 2.70 µmol L^{-1} m day^{-1}, indicating that upward oxygen transport from below can exceed the ventilation from above, especially during periods of strong salt-finger activity. Notably, salt fingering dominated diapycnal mixing across the lower oxycline, contributing 83%, 79%, and 66% on average of the total diffusivity in January 2020, July 2021, and October 2022, respectively. This substantial and variable influence underscores the importance of double-diffusive processes in sustaining upward oxygen fluxes, particularly during periods of enhanced thermohaline stratification. Despite weaker vertical oxygen gradients at depth, the elevated diffusivities associated with salt fingering enabled oxygen transport into the OMZ core that was comparable in magnitude to fluxes driven by shear-induced turbulence at the upper boundary.

Discussion

Microstructure observations and tracer release experiments have consistently shown that shear-induced turbulence is highly intermittent, displaying pronounced spatial and temporal variability[18,21,44]. Our measurements off central Chile corroborate this pattern, revealing relatively weak turbulence intensities overall. Median dissipation rates typically ranged between 10^{-9} and 10^{-8} m^2 s^{-3} for ε, and between 10^{-8} and 10^{-7} K^2 s^{-1} for χ, with intermittent and localized instances exceeding 10^{-7} for ε, and 10^{-6} for χ (Fig. 5). This is noteworthy given the study site's position on the upper continental slope, a region commonly associated with internal wave activity and elevated mixing[48]. However, our measurements represent a localized virtual-mooring-like perspective, with limited horizontal displacement and no direct sampling of the near-bottom boundary layer, where topography-induced mixing may occur. Furthermore, our temporal coverage does not resolve diurnal or semidiurnal tidal cycles that could modulate internal wave energy. These factors likely contribute to the generally low turbulence levels observed, underscoring the need for future observations capable of resolving both spatial and tidal variability along this slope. The generally low turbulence levels we observed are consistent with those reported for other eastern boundary systems[49] and fall toward the lower end of the range reported for similarly stratified environments in other ocean basins[46]. Such limited diapycnal mixing, when combined with high subsurface respiration rates at the upper oxycline, likely plays an important role in maintaining the sharp vertical structure and persistence of the pronounced OMZ off central Chile[2,5]. At the same time, horizontal processes, including along-isopycnal advection, intra-thermocline eddies, and vertical shear of horizontal currents, also contribute to shaping the observed oxygen structure, operating over different timescales than vertical turbulent exchange. Future coordinated observations resolving both lateral and vertical variability are needed to quantify their relative importance.

Despite the modest magnitude of shear-driven diapycnal mixing, accurately quantifying these rates remains crucial for constraining vertical diffusivities and regional oxygen budgets. In July 2021 and October 2022, Ri exceeded unity in 80% and 91% of cases, respectively (where ADCP was available; Supplementary Note 5). Following St. Laurent and Schmitt[21], who demonstrated that the density ratio R_ρ exerts a stronger control on double-

Table 2 | Diapycnal-mixing characteristics and oxygen-transport estimates for each density interval

$N_\circ$	P_t	P_f	$K_{st} \times 10^{-5}$ ($m^2\ s^{-1}$)	$K_{sf} \times 10^{-5}$ ($m^2\ s^{-1}$)	$K \times 10^{-5}$ ($m^2\ s^{-1}$)	$\partial O_2/\partial z$ ($\mu mol\ L^{-1}\ m^{-1}$)	ϕ_{O_2} ($\mu mol\ m\ L^{-1}\ day^{-1}$)	$-\nabla_z\left(\phi_{O_2}\right)$ ($\mu mol\ L^{-1}\ day^{-1}$)
January 2020								
(1)	1	0	1.4 ± 0.4		1.4 ± 0.4	1.16 ± 0.09	−1.40 ± 0.41	0.06 ± 0.02
(2)	1	0	2.84 ± 0.49		2.84 ± 0.49	1.24 ± 0.04	−3.03 ± 0.54	0.53 ± 0.27
(3)	1	0	5.32 ± 2.28		5.32 ± 2.28	3.35 ± 0.17	−15.39 ± 6.64	−0.27 ± 0.15
(4)	1	0	6.9 ± 0.94		6.9 ± 0.94	0.56 ± 0.06	−3.37 ± 0.59	−0.10 ± 0.04
(5)	0.74	0.26	3.7 ± 0.18	423.13 ± 238.02	112.8 ± 61.88	−0.07 ± 0.01	6.95 ± 3.96	0.08 ± 0.06
(6)	0.74	0.26	1.63 ± 0.15	8.28 ± 1.94	3.36 ± 0.52	−0.26 ± 0.01	0.75 ± 0.12	−0.06 ± 0.03
(7)	0.73	0.27	2.53 ± 0.12	43.99 ± 16.05	13.72 ± 4.34	−0.77 ± 0.01	9.11 ± 2.88	
July 2021								
(1)	1	0	5.83 ± 1.96		5.83 ± 1.72	1.62 ± 0.12	−8.15 ± 2.81	−0.21 ± 0.11
(2)	1	0	2.45 ± 0.66		2.45 ± 0.54	2.58 ± 0.10	−5.48 ± 1.49	0.44 ± 0.24
(3)	1	0	7.95 ± 3.52		7.95 ± 2.83	2.36 ± 0.10	−16.19 ± 7.21	−0.20 ± 0.12
(4)	1	0	4.91 ± 0.35		4.91 ± 0.35	0.48 ± 0.05	−2.04 ± 0.25	−0.04 ± 0.01
(5)	0.83	0.17	16.5 ± 1.15	549.19 ± 157.7	107.1 ± 28.89	−0.02 ± 0.00	2.11 ± 0.54	−0.02 ± 0.01
(6)	0.81	0.19	3.98 ± 0.39	94.49 ± 48.53	21.18 ± 10.06	−0.20 ± 0.00	3.65 ± 1.59	−0.02 ± 0.01
(7)	0.81	0.19	3.62 ± 0.39	27.54 ± 7.85	8.17 ± 14.7	−0.71 ± 0.02	5.00 ± 0.94	
October 2022								
(1)	1	0	0.71 ± 0.06		0.71 ± 0.06	0.30 ± 0.07	−0.18 ± 0.05	0.06 ± 0.01
(2)	1	0	0.81 ± 0.07		0.81 ± 0.07	2.33 ± 0.06	−1.63 ± 0.15	0.01 ± 0.01
(3)	1	0	0.72 ± 0.08		0.72 ± 0.08	2.95 ± 0.07	−1.83 ± 0.20	−0.02 ± 0.01
(4)	1	0	1.26 ± 0.07		1.26 ± 0.07	1.11 ± 0.06	−1.21 ± 0.09	−0.01 ± 0.01
(5)	1	0	2.29 ± 0.16		2.29 ± 0.16	0.33 ± 0.02	−0.65 ± 0.06	−0.06 ± 0.02
(6)	0.85	0.15	5.42 ± 2.7	134.4 ± 70.21	24.76 ± 10.78	−0.18 ± 0.01	3.89 ± 1.70	0.03 ± 0.02
(7)	0.82	0.18	1.49 ± 0.12	6.92 ± 1.27	2.47 ± 0.25	−0.71 ± 0.00	1.51 ± 0.15	

Based on data from January 2020, July 2021, and October 2022. Columns: (ii)–(iii) percentage contribution of shear-driven turbulence (P_t) and salt-finger mixing (P_f); (iv)–(vi) diapycnal diffusivities associated with shear turbulence, salt fingers, and the combined (net) estimate; (vii) mean vertical dissolved-oxygen gradient; (viii) diapycnal oxygen flux; and (ix) vertical divergence of oxygen flux. Uncertainties for (iv)–(vi) were derived by error propagation (Eq. S9–S12). Values in (vii) are interval means from degree−1 least-squares fits, with "±" indicating the standard error of the fit. Errors for (viii) and (ix) were obtained by standard propagation of the uncertainties from the preceding variables.

diffusive efficiency, we assumed $Ri > 1$ for the January 2020 campaign and for depths below the ADCP range in the later cruises, where direct current measurements were unavailable. Consequently, salt-finger contributions to mixing below the ADCP coverage are interpreted as inferred from thermohaline structure (R_ρ criteria) rather than directly constrained by velocity shear. This assumption may overestimate the salt-finger diffusivity between 10 and 20%, based on inter-year comparisons and density intervals where Ri was available.

While this extrapolation introduces some uncertainty, it does not alter the overall picture of a stratified lower oxycline that favors double-diffusive convection over shear-driven turbulence. In contrast to turbulence driven by shear, double-diffusive processes such as salt fingering are driven by the thermohaline stratification, which in our study area exhibits remarkable temporal stability (Figs. 4a–c and S4). This persistent background stratification maintains conditions favorable for salt-finger activity, enabling a continuous contribution to diapycnal diffusivity. Notably, beneath the salinity maximum associated with the ESSW, salt-finger mixing occurred in approximately 15–27% of the observations ($P_f = 0.15 - 0.27$). When present, salt-finger-induced diffusivities were up to two orders of magnitude greater than those generated by shear-driven turbulence, and combined with the weighting effect, contribute on average up to 83% of the total diapycnal diffusivity at the lower oxycline. These results underscore the potentially dominant role of double diffusion in ventilating stratified OMZs, particularly in regions where thermohaline gradients remain stable over seasonal to interannual timescales[20–22].

Given the critical role of mixing in regulating oxygen budgets within OMZs[10,16,50], our results underscore the importance of salt-finger-driven mixing as a persistent and substantial mechanism of diapycnal ventilation from below in the ESP-OMZ. Although shear-induced turbulence has traditionally been viewed as the dominant driver of vertical oxygen transport, particularly across the upper oxycline where sharp gradients prevail, our data reveal that vertical diffusivities in the lower oxycline, driven largely by salt fingering, often exceed those in the upper layers despite smoother oxygen gradients. The resulting diapycnal oxygen fluxes at the lower boundary (5.60, 3.59, and 2.70 $\mu mol\ L^{-1}\ m\ day^{-1}$ for January 2020, July 2021, and October 2022, respectively) are comparable in magnitude to those across the upper oxycline (–7.26, –7.9, and –1.33 $\mu mol\ L^{-1}\ m\ day^{-1}$), where shear-driven turbulence dominates. This suggests that bottom-up ventilation, mediated by double-diffusive processes, can rival or even exceed top-down supply in certain periods. Such fluxes are nontrivial when integrated over the OMZ's spatial extent and may represent an important component of its oxygen budget. Comparable enhancements of turbulent diffusivity below the OMZ core were also reported by Fischer et al.[24] in the tropical North Atlantic, who demonstrated the potential influence of double diffusion using a prescribed salt-finger diffusivity coefficient (K_θ). While our analysis similarly points to substantial double-diffusive contributions, it was constrained by incomplete shear observations and by inferring stability solely from R_ρ. Together, these studies illustrate both the significance of double diffusion in OMZ ventilation and the limitations of current observational approaches, underscoring the need for dedicated experiments that

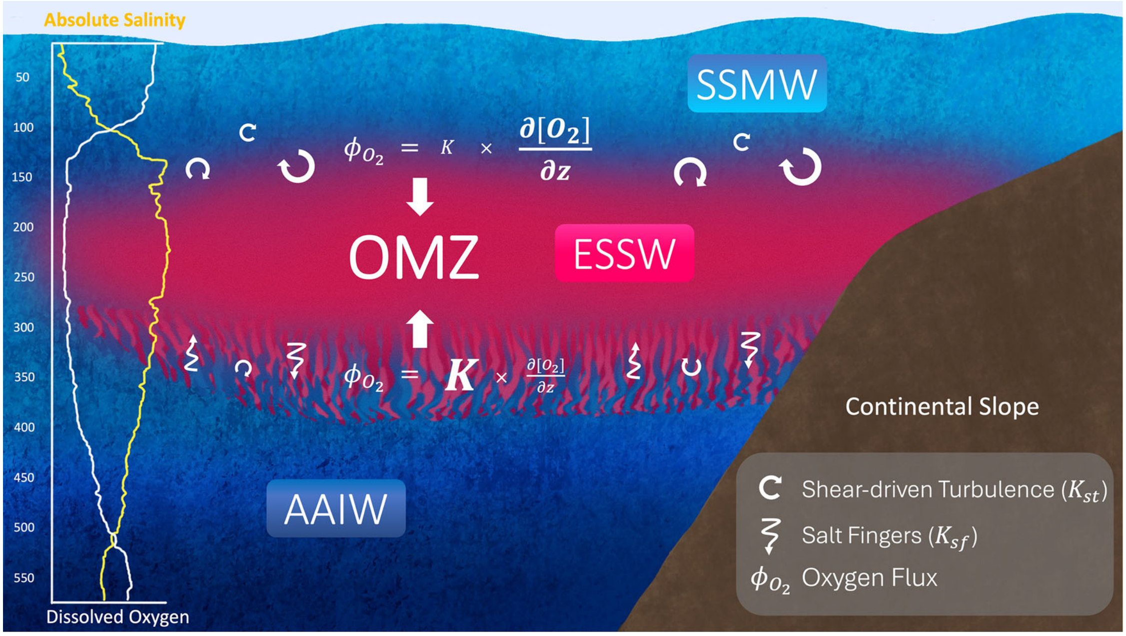

Fig. 7 | Conceptual model of diapycnal oxygen transport across the southern eastern South Pacific oxygen minimum zone. Schematic representation of the diapycnal dissolved oxygen fluxes (ϕ_{O_2}) along the southern ESP-OMZ. The core of the ESSW lies between the SSMW above and the AAIW below. A representative dissolved oxygen and salinity profile (white and yellow lines, respectively) shows the inverse relationship between the two. The upper oxycline is dominated by shear-driven turbulence (K_{st}), and strong stratification suppresses vertical mixing, resulting in low diffusivities where sharp oxygen gradients are present. At the lower oxycline, where gradients are weaker, the thermohaline contrasts allow both double-diffusive instabilities and shear-driven turbulence to contribute ($K_{st} + K_{sf}$). This combination results in comparable diapycnal oxygen fluxes across both oxyclines, reflecting a compensatory relationship between mixing intensity and the vertical DO gradient.

jointly resolve ε, χ, and shear to better quantify the coupling between shear-driven and double-diffusive mixing processes.

Figure 7 synthesizes the dominant processes governing diapycnal mixing dynamics within the Central Chile OMZ. In the upper oxycline, mixing is primarily driven by shear-induced turbulence, characterized by lower diffusivities but steeper vertical oxygen gradients. In contrast, beneath the OMZ core, particularly at the interface between the ESSW and AAIW, salt fingering emerges as a first-order contributor to mixing, characterized by enhanced diffusivities but weaker oxygen gradients. This inverse relationship between diffusivity and gradient results in comparable diapycnal oxygen fluxes across both oxyclines, highlighting a compensatory relationship between mixing intensity and oxygen gradient. These findings challenge the prevailing view of OMZ ventilation as primarily upper-boundary driven[3,50] and indicate that double-diffusive mixing, though often overlooked, provides a sustained, physically distinct, and climatically relevant oxygen source to the OMZ core. Incorporating double-diffusive processes into diapycnal diffusivity parameterizations for the ESP-OMZ, particularly across transitional layers such as the ESSW–AAIW interface, is essential for accurately modeling and monitoring OMZ dynamics and preventing underestimation of oxygen supply and its variability in a changing ocean.

Although our observations represent brief snapshots, they span multiple years, seasons, and upwelling regimes, providing a valuable perspective on the mixing processes active near the OMZ core. Several limitations, however, must be acknowledged. The vertical extent of our velocity measurements was constrained by the depth range of ADCP coverage, limiting our ability to fully resolve double diffusive-driven turbulence throughout the water column. This constraint likely influenced the relative weighting between shear-driven turbulence and salt-finger contributions (P_t and P_f), particularly in deeper layers where salt-finger instability appears to dominate. Furthermore, the inherently intermittent and spatially patchy nature of shear-induced mixing, especially in stratified boundary layers, poses a significant challenge for capturing representative statistics from short-duration campaigns. Despite these limitations, the consistent detection of both shear- and salt-finger-favorable regimes across all three deployments points to a sustained interplay between these mechanisms at the OMZ lower boundary. Future studies should aim to characterize the spatial and temporal variability of these processes more comprehensively, including the role of thermohaline intrusions and interleaving in triggering episodic salt-finger activity. As climate change alters the large-scale stratification and water mass properties that underpin these instabilities, understanding how the balance between shear- and double diffusive-driven mixing may shift will be essential for predicting the future evolution of OMZs.

While our study focuses on the southern extent of the ESP-OMZ, analysis of historical data suggests that conditions conducive to salt-finger formation are widespread across much of the eastern South Pacific. To evaluate the broader relevance of salt-finger mixing in other eastern boundary OMZs, we examined Turner angles computed from historical CTD profiles in the California, Canary, and Benguela upwelling systems (Supplementary Note 2; Figs. S2 and S3), all associated with moderate to strong OMZs. Unlike the ESP, the California OMZ displays Turner angles largely unfavorable for double-diffusive instabilities, likely due to the absence of adjacent subpolar-origin, low-salinity waters necessary for salt fingering. In contrast, the Canary and Benguela OMZs, though generally weaker (i.e., higher DO concentrations relative to the ESP-OMZ), exhibit Turner angles consistently within the favorable range across the OMZ depth interval, suggesting that double-diffusive mixing may contribute meaningfully to their ventilation. Interestingly, despite structural similarities between the Benguela and ESP-OMZs, the Benguela system lacks a pronounced subsurface salinity maximum akin to the ESSW, resulting in more vertically uniform Turner angle profiles.

Even in regions where the OMZ is not coincident with a salinity core, these processes can play a key role. For example, the Arabian Sea OMZ also exhibits conditions favorable for salt fingering. In contrast to the ESP-OMZ, where salt fingering dominates the lower oxycline, the Arabian Sea OMZ displays Turner angles exceeding 45° near the upper oxycline, where high-salinity Persian Gulf water intrudes above the oxygen-depleted core[23,51]. While the observed thermohaline structure suggests a potential role for double-diffusive mixing in vertical ventilation, its contribution to oxygen fluxes in this region remains to be quantified.

Beyond highlighting the role of salt fingers in enhancing diapycnal oxygen transport at the lower OMZ boundary, our findings emphasize the importance of interactions with other dynamical processes. Isopycnal mixing driven by mesoscale and submesoscale stirring exerts a substantial influence on regional oxygen distributions[3,32,34,35] and may modulate both the intensity and vertical structure of diapycnal mixing. In particular, the coincidence of lateral intrusions with the density range where salt-finger-favorable Turner angle values are observed underscores the potential for thermohaline interleaving to trigger or enhance double-diffusive instabilities. These processes likely interact to create fine-scale stratification that shapes the spatiotemporal variability of vertical oxygen transport within the lower boundary of the ESP-OMZ. Understanding how these mechanisms co-evolve and the extent to which horizontal variability governs vertical exchange will be essential for constraining the future evolution of OMZ ventilation under changing climate conditions. A comprehensive understanding of OMZ dynamics, therefore, requires integrative approaches that explicitly address the coupling between isopycnal and diapycnal processes. Continued progress will depend on strategies that combine high-resolution observations, targeted process studies, and next-generation coupled models capable of resolving fine-scale double-diffusive and mesoscale interactions. Such efforts will be critical for improving predictions of OMZ behavior in a rapidly deoxygenating ocean.

Data and methods

Data

The data used in this study were collected along the continental slope off Central Chile (~36.5°S) during three oceanographic cruises conducted aboard the R/V Kay-Kay-II of the University of Concepción (Fig. 1a–c). Hydrographic and microstructure measurements were acquired during all three cruises, January 2020, July 2021, and October 2022, using a Sea-bird electronics SBE 25 CTD equipped with an SBE 43 DO sensor, and a Vertical Microstructure Profiler (VMP-250; Table S1).

In the second cruise (July 2021), we expanded our observations by including a drifting array instrumented with three Acoustic Doppler Current Profilers (ADCPs; Teledyne-RDI at 1200, 600, and 300 kHz) for detailed horizontal current measurements. In the third cruise (October 2022), similar instrumentation was used; however, the ADCP array was deployed as a moored system near 600 m depth, and the 1200 kHz ADCP was excluded from this deployment (Table S2). A detailed summary of the instrumentation and data collected during each survey is provided in Supplementary Tables S1 and S2.

Microstructure data were acquired using a VMP-250 (Rockland Scientific International Inc) equipped with high-resolution (512 Hz) horizontal shear velocity and temperature sensors, enabling calculation of the turbulent kinetic energy dissipation rate (ε) and thermal variance dissipation rate (χ). The profiler also included lower-resolution (64 Hz) sensors for pressure, temperature, conductivity, turbidity, and chlorophyll. The instrument was deployed in free-fall mode, descending at ~0.7 m s^{-1} and reaching depths up to 1000 m. Each deployment consisted of three consecutive vertical profiles.

To contextualize the in situ observations, we used a suite of complementary datasets. Sea surface temperature patterns were analyzed using the multi-scale ultra-high resolution (MUR-GHRSST) product[52], while surface circulation and mesoscale variability were characterized with sea surface height data from the SSALTO/DUACS Near-Real-Time level-4 product and its derived variables (https://doi.org/10.48670/moi-00148). Wind conditions preceding and during each cruise were characterized using hourly ERA5 reanalysis data[53]. Wind stress conditions for upwelling were computed following standard methodologies[54] (see also Supplementary Note 1).

The broader spatial and temporal context of the OMZ along the Peruvian and Chilean margins was assessed using historical CTD data from the World Ocean Database (WOD[55]), covering the period 1980–2022 (Fig. 3b). In addition, local conditions at 36.5°S were examined using high-resolution CTD-O profiles collected during eight glider transects conducted across different seasons between 2010 and 2012, extending approximately 180 km offshore (Fig. 3c, d; See also Supplementary Notes 2 and 3; Supplementary Figs. S2–4).

Preliminary analysis indicated enhanced salt-finger mixing at the interface between ESSW and Antarctic intermediate water (AAIW), coinciding with the lower oxycline of the OMZ. Accordingly, ADCP observations were focused primarily on the 100–300 m depth range. These velocity measurements, combined with simultaneous CTD profiles, were used to compute gradient Richardson numbers (*Ri*) and to evaluate local mixing regimes (see "Methods").

Methods

To distinguish the stability of the water column to double diffusion processes we used Turner angles *Tu*, defined as Ruddick[56] $Tu = \tan^{-1}\left(\alpha\frac{\partial\Theta}{\partial z} - \beta\frac{\partial S}{\partial z}, \alpha\frac{\partial\Theta}{\partial z} + \beta\frac{\partial S}{\partial z}\right)$. Turner angles clearly discriminate double-diffusive regimes: values between $+45°$ and $+90°$ indicate salt-finger conditions, values from $-45°$ to $-90°$ indicate diffusive convection, while angles within ±45° represent stable stratification with respect to both temperature and salinity[22].

Diapycnal diffusivity was estimated following the framework proposed by St. Laurent and Schmitt[21], which distinguishes two primary regimes of mixing: shear-driven turbulence and salt fingering. The authors suggest that salt-finger mixing is effective within a specific stability parameter space, defined by the density ratio, and the gradient Richardson number, $\mathrm{sfs} = [1 < R_\rho < 2, Ri > 1]$. These parameters are expressed as $R_\rho = \frac{\alpha\Theta_z}{\beta S_z}$, and $Ri = \frac{N^2}{|U_z|^2}$, where α is the thermal expansion coefficient, Θ_z is the vertical gradient of conservative temperature, β is the haline contraction coefficient, S_z is the vertical gradient of absolute salinity, N^2 is the squared buoyancy frequency, and U_z is the vertical shear of horizontal velocity. All vertical gradients are computed with respect to pressure (depth), under the assumption of locally horizontal isopycnals.

The parameter space for salt-finger favorable conditions sfs, is based on theoretical and experimental evidence suggesting reduced double-diffusive instability at higher density ratios and suppression by shear instability at $Ri < 1$. The sfs was calculated within 7 potential density intervals selected from temperature-salinity diagrams, these intervals were chosen to represent the different conditions related to the transition of the water masses in the region, with an increase in resolution near the salt maximum in the core of the OMZ (see Fig. 4a). In this way, it was possible to estimate the relative contribution to mixing of salt fingers (P_f), defined as the proportion of observations meeting the *sfs* criterion within each density interval, and of shear-driven turbulence ($P_t = 1 - P_f$).

Local values of R_ρ were derived from VMP-CTD profiles, computed at a vertical resolution of 2 m. The *Ri* values were calculated using N^2 at the same vertical resolution, combined with a representative vertical shear profile U_z, which was obtained by temporally averaging the ADCP measurements (when available) over the duration of the VMP-250 descent; typically between 10 and 15 min. All profiles were subsequently linearly interpolated to a uniform vertical resolution of 2 m (see supplementary Note 5 for further details).

The fraction of mixing attributed to salt fingering and to shear-driven turbulence were evaluated following the approach of St. Laurent and Schmitt[21] using the sfs space. Because *Ri* requires shear from ADCP data, P_t and P_f were directly determined only over the ~150–300 m depth range where reliable velocity data were available. Below this range, the relative contribution of salt fingering was inferred just from hydrographic conditions, specifically the persistence of $1 < R_\rho < 2$ and assuming $Ri > 1$.

In this study, bulk diffusivity profiles were performed for the three cruises (January 2020, July 2021, and October 2022) within the 7 distinct potential density intervals (Fig. 4 and Table 1). Within each interval, mean values of squared buoyancy frequency ($\bar{N}^2$), conservative temperature gradient ($\bar{\Theta}_z$), vertical absolute salinity gradient ($\bar{S}_z$), and density ratio ($\bar{R}_\rho$) were estimated using least-squares fits (see Supplementary Note 5 for further details).

Shear-driven diffusivity (K_{st}) was estimated using the Osborn[57] parametrization

$$K_{st} = \Gamma^{(t)} \frac{\langle \varepsilon \rangle}{\bar{N}^2}, \quad (1)$$

where $\Gamma^{(t)}$ is the mixing efficiency, and $\langle \varepsilon \rangle$ is the ensemble-averaged dissipation rate of turbulent kinetic energy within each σ_t interval, derived from VMP microstructure observations (see Supplementary Note 4 for further details about how the dissipation rates of ε and χ were estimated). An experimentally supported upper threshold value of $\Gamma^{(t)} = 0.2$ was adopted[18,58].

Salt-finger diffusivity (K_{sf}) was calculated following Hamilton et al.[59], based on the heat diffusivity (K_T) formulation by Osborn and Cox[60]:

$$K_T = \frac{\langle \chi \rangle}{2\bar{\Theta}_z^2}, \quad (2)$$

where $\langle \chi \rangle$ is the ensemble average thermal variance dissipation rate within each σ_t interval associated with salt fingers also estimated from microstructure observations. $\langle \varepsilon \rangle$ and $\langle \chi \rangle$ correspond to the ensemble means over independent, non-overlapping 2-m segments within each density interval, and their uncertainty is the bootstrap standard error (standard deviation of the bootstrap distribution of the mean) computed from 8 M resamples per interval (see Note 5 for details). Subsequently, salt-finger diffusivity was determined as:

$$K_{sf} = \frac{\bar{R}_\rho}{r} K_T, \quad (3)$$

with $r = 0.6$ representing the heat to salt buoyancy-flux ratio (St. Laurent and Schmitt[21]). The net diapycnal diffusivity (K) was then computed by weighting the shear-driven, and salt-finger diffusivities according to their prevalence fractions (P_t, P_f) at each depth interval:

$$K = P_t(K_{st}) + P_f(K_{sf}), \quad (4)$$

The turbulent kinetic energy dissipation (ε) was computed from VMP data using the Rockland Scientific ODAS toolbox (v4.5.1) enhanced with additional recommendations of the ATOMIX group[61] (Fig. S5), and the thermal variance dissipation (χ) rates were computed applying methods described by Bluteau et al.[62] (see also Supplementary Note 4).

Finally, vertical DO fluxes ϕ_{O_2}, were estimated using Fick's law:

$$\phi_{O_2} = -K \times \frac{\partial [O_2]}{\partial z}, \quad (5)$$

where the oxygen vertical gradient ($\partial [O_2] / \partial z$) was derived from DO profiles measured by the CTD-O using least-squares linear fitting within each density interval. The respective standard errors for the diffusivities are described in the Note 5 (Eq. S9–S12).

Data availability

The CTD-O and ADCP data used to calculate oxygen gradients and Richardson numbers, as well as the VMP microstructure data used to derive turbulent kinetic energy dissipation and temperature variance dissipation rates, are available on Zenodo (https://doi.org/10.5281/zenodo.15755810).

Code availability

All codes used for data processing, analysis, and figure generation in this study are publicly available on Zenodo at https://doi.org/10.5281/zenodo.15754867.

Received: 17 July 2025; Accepted: 6 January 2026;

References

1. Stramma, L., Johnson, G. C., Sprintall, J. & Mohrholz, V. Expanding oxygen-minimum zones in the tropical oceans. *Science* **320**, 655–658 (2008).
2. Karstensen, J., Stramma, L. & Visbeck, M. Oxygen minimum zones in the eastern tropical Atlantic and Pacific oceans. *Prog. Oceanogr.* **77**, 331–350 (2008).
3. Lévy, M., Resplandy, L., Palter, J. B., Couespel, D. & Lachkar, Z. The crucial contribution of mixing to present and future ocean oxygen distribution. in *Ocean Mixing* (eds Meredith, M. & Naveira Garabato, A.) 329–344 (Elsevier, 2022).
4. Köhn, E. E., Greatbatch, R. J., Brandt, P. & Claus, M. The formation and ventilation of an oxygen minimum zone in a simple model for latitudinally alternating zonal jets. *Ocean Sci.* **20**, 1281–1290 (2024).
5. Fuenzalida, R., Schneider, W., Garcés-Vargas, J., Bravo, L. & Lange, C. Vertical and horizontal extension of the oxygen minimum zone in the eastern South Pacific Ocean. *Deep Sea Res. Part II* **56**, 992–1003 (2009).
6. Cavan, E. L., Trimmer, M., Shelley, F. & Sanders, R. Remineralization of particulate organic carbon in an ocean oxygen minimum zone. *Nat. Commun.* **8**, 14847 (2017).
7. Laffoley, D. & Baxter, J. M. (eds) *Ocean Deoxygenation: Everyone's Problem* (IUCN, 2019).
8. Oschlies, A. A committed fourfold increase in ocean oxygen loss. *Nat. Commun.* **12**, 2307 (2021).
9. Busecke, J. J., Resplandy, L., Ditkovsky, S. J. & John, J. G. Diverging fates of the Pacific Ocean oxygen minimum zone and its core in a warming world. *AGU Adv.* **3**, e2021AV000470 (2022).
10. Ditkovsky, S. & Resplandy, L. Unifying future ocean oxygen projections using an oxygen water mass framework. *J. Geophys. Res. Oceans* **130**, e2025JC022333 (2025).
11. Gallo, N. D. & Levin, L. A. Fish ecology and evolution in the world's oxygen minimum zones and implications of ocean deoxygenation. in *Advances in Marine Biology* Vol. 74 (ed Curry, B. E.) 117–198 (Academic Press, 2016).
12. Wishner, K. F., Seibel, B. & Outram, D. Ocean deoxygenation and copepods: coping with oxygen minimum zone variability. *Biogeosciences* **17**, 2315–2339 (2020).
13. Ulloa, O., Canfield, D. E., DeLong, E. F., Letelier, R. M. & Stewart, F. J. Microbial oceanography of anoxic oxygen minimum zones. *Proc. Natl. Acad. Sci. USA* **108**, 15996–16003 (2012).
14. Beman, J. M. et al. Substantial oxygen consumption by aerobic nitrite oxidation in oceanic oxygen minimum zones. *Nat. Commun.* **12**, 7381 (2021).
15. Ma, J. et al. Different fates of particulate matters driven by marine hypoxia: a case study of oxygen minimum zone in the western Pacific. *Mar. Environ. Res.* **200**, 106648 (2024).
16. Couespel, D., Lévy, M. & Bopp, L. Major contribution of reduced upper ocean oxygen mixing to global ocean deoxygenation in an Earth System Model. *Geophys. Res. Lett.* **46**, 12239–12249 (2019).
17. Frajka-Williams, E., Brearley, J. A., Nash, J. D. & Whalen, C. B. New technological frontiers in ocean mixing. in *Ocean Mixing* (eds Meredith, M. & Naveira Garabato, A.) 345–361 (Elsevier, 2022).
18. Gregg, M. C., D'Asaro, E. A., Riley, J. J. & Kunze, E. Mixing efficiency in the ocean. *Annu. Rev. Mar. Sci.* **10**, 443–473 (2018).

19. Alford, M. H., MacKinnon, J. A., Simmons, H. L. & Nash, J. D. Near-inertial internal gravity waves in the ocean. *Annu. Rev. Mar. Sci.* **8**, 95–123 (2016).
20. Radko, T. *Double-Diffusive Convection* (Cambridge University Press, 2013).
21. St. Laurent, L. & Schmitt, R. W. The contribution of salt fingers to vertical mixing in the North Atlantic tracer release experiment*. *J. Phys. Oceanogr.* **29**, 1404–1424 (1999).
22. You, Y. A global ocean climatological atlas of the Turner angle: implications for double-diffusion and water-mass structure. *Deep Sea Res. Part I* **49**, 2075–2093 (2002).
23. Font, E. et al. Ventilation of the Arabian Sea oxygen minimum zone by Persian Gulf water. *J. Geophys. Res. Oceans* **129**, e2023JC020668 (2024).
24. Fischer, T. et al. Diapycnal oxygen supply to the tropical north Atlantic oxygen minimum zone. *Biogeosciences* **10**, 5079–5093 (2013).
25. Kamykowski, D. & Zentara, S.-J. Hypoxia in the world ocean as recorded in the historical data set. *Deep Sea Res. Part A* **37**, 1861–1874 (1990).
26. Thamdrup, B., Dalsgaard, T. & Revsbech, N. P. Widespread functional anoxia in the oxygen minimum zone of the eastern South Pacific. *Deep Sea Res. Part I* **65**, 36–45 (2012).
27. Revsbech, N. P. et al. Determination of ultra-low oxygen concentrations in oxygen minimum zones by the STOX sensor. *Limnol. Oceanogr. Methods* **7**, 371–381 (2009).
28. Linford, P. et al. Recent deoxygenation of Patagonian fjord subsurface waters connected to the Peru–Chile undercurrent and equatorial subsurface water variability. *Glob. Biogeochem. Cycles* **37**, e2022GB007688 (2023).
29. Leth, O., Shaffer, G. & Ulloa, O. Hydrography of the eastern South Pacific ocean: results from the Sonne 102 cruise, May–June 1995. *Deep Sea Res. Part II* **51**, 2349–2369 (2004).
30. Silva, N., Rojas, N. & Fedele, A. Water masses in the Humboldt current system: properties, distribution, and the nitrate deficit as a chemical water mass tracer for equatorial subsurface water off Chile. *Deep Sea Res. Part II* **56**, 1004–1020 (2009).
31. Llanillo, P. et al. Meridional and zonal changes in water properties along the continental slope off central and northern Chile. *Cien. Mar.* **38**, 307–332 (2011).
32. Llanillo, P. J., Pelegrí, J. L., Talley, L. D., Peña-Izquierdo, J. & Cordero, R. R. Oxygen pathways and budget for the eastern South Pacific oxygen minimum zone. *J. Geophys. Res. Oceans* **123**, 1722–1744 (2018).
33. Karstensen, J. Formation of the South Pacific shallow salinity minimum: a southern ocean pathway to the tropical Pacific. *J. Phys. Oceanogr.* **34**, 2398–2412 (2004).
34. Bettencourt, J. H. et al. Boundaries of the Peruvian oxygen minimum zone shaped by coherent mesoscale dynamics. *Nat. Geosci.* **8**, 937–940 (2015).
35. Pizarro-Koch, M. et al. Seasonal variability of the southern tip of the oxygen minimum zone in the eastern South Pacific (30°-38°S): a modeling study. *J. Geophys. Res. Oceans* **124**, 8574–8604 (2019).
36. Pizarro-Koch, M. et al. On the interpretation of changes in the subtropical oxygen minimum zone volume off Chile during two La Niña events (2001 and 2007). *Front. Mar. Sci.* **10**, 1155932 (2023).
37. Vergara, O., Dewitte, B., Ramos, M. & Pizarro, O. Vertical energy flux at ENSO time scales in the subthermocline of the southeastern Pacific. *J. Geophys. Res. Oceans* **122**, 6011–6038 (2017).
38. Pizarro, O. et al. Underwater glider observations in the oxygen minimum zone off central Chile. *Bull. Am. Meteorol. Soc.* **97**, 1783–1789 (2016).
39. Li, J. & Yang, Y. Thermohaline interleaving induced by horizontal temperature and salinity gradients from above. *J. Fluid Mech.* **927**, A12 (2021).
40. Pietri, A. et al. Finescale vertical structure of the upwelling system off southern Peru as observed from glider data. *J. Phys. Oceanogr.* **43**, 631–646 (2013).
41. Jan, S., Wang, S.-H., Yang, K.-C., Yang, Y. J. & Chang, M.-H. Glider observations of interleaving layers beneath the Kuroshio primary velocity core east of Taiwan and analyses of underlying dynamics. *Sci. Rep.* **9**, 11094 (2019).
42. Ruddick, B. & Richards, K. Oceanic thermohaline intrusions: observations. *Prog. Oceanogr.* **56**, 499–527 (2003).
43. Shcherbina, A. Y., Gregg, M. C., Alford, M. H. & Harcourt, R. R. Characterizing thermohaline intrusions in the North Pacific subtropical frontal zone. *J. Phys. Oceanogr.* **39**, 2735–2756 (2009).
44. Gregg, M. C. Diapycnal mixing in the thermocline: a review. *J. Geophys. Res.* **92**, 5249–5286 (1987).
45. Schafstall, J., Dengler, M., Brandt, P. & Bange, H. Tidal-induced mixing and diapycnal nutrient fluxes in the Mauritanian upwelling region. *J. Geophys. Res. Oceans* **115**, C10013 (2010).
46. Waterhouse, A. F. et al. Global patterns of diapycnal mixing from measurements of the turbulent dissipation rate. *J. Phys. Oceanogr.* **44**, 1854–1872 (2014).
47. Arcos-Pulido, M. et al. Diapycnal nutrient fluxes on the northern boundary of Cape Ghir upwelling region. *Deep Sea Res. Part I* **84**, 100–109 (2014).
48. Aguirre, C., Pizarro, O. & Sobarzo, M. Observations of semidiurnal internal tidal currents off central Chile (36.6 S). *Cont. Shelf Res.* **30**, 1562–1574 (2010).
49. Lozovatsky, I., Shearman, K., Pirro, A. & Fernando, H. J. S. Probability distribution of turbulent kinetic energy dissipation rate in stratified turbulence: microstructure measurements in the southern California bight. *J. Geophys. Res. Oceans* **124**, 4591–4604 (2019).
50. Brandt, P. et al. On the role of circulation and mixing in the ventilation of oxygen minimum zones with a focus on the eastern tropical North Atlantic. *Biogeosciences* **12**, 489–512 (2015).
51. Queste, B. Y., Vic, C., Heywood, K. J. & Piontkovski, S. A. Physical controls on oxygen distribution and denitrification potential in the north west Arabian Sea. *Geophys. Res. Lett.* **45**, 4143–4152 (2018).
52. NASA/JPL. *GHRSST Level 4 MUR Global Foundation Sea Surface Temperature Analysis (v4.1)* https://doi.org/10.5067/GHGMR-4FJ04 (NASA Physical Oceanography Distributed Active Archive Center, 2015).
53. Hersbach, H. et al. The ERA5 global reanalysis. *Q. J. R. Meteorol. Soc.* **146**, 1999–2049 (2020).
54. Yelland, M. & Taylor, P. K. Wind stress measurements from the open ocean. *J. Phys. Oceanogr.* **26**, 541–558 (1996).
55. Boyer, T. P. et al. *World ocean database 2009* (2009).
56. Ruddick, B. A practical indicator of the stability of the water column to double-diffusive activity. *Deep Sea Res. Part A* **30**, 1105–1107 (1983).
57. Osborn, T. R. Estimates of the local rate of vertical diffusion from dissipation measurements. *J. Phys. Oceanogr.* **10**, 83–89 (1980).
58. Thorpe, S. A. *The Turbulent Ocean* (Cambridge University Press, 2005).
59. Hamilton, J. M., Oakey, N. S. & Kelley, D. E. Salt finger signatures in microstructure measurements. *J. Geophys. Res. Oceans* **98**, 2453–2460 (1993).
60. Osborn, T. R. & Cox, C. S. Oceanic fine structure. *Geophys. Fluid Dyn.* **3**, 321–345 (1972).
61. Lueck, R. et al. Best practices recommendations for estimating dissipation rates from shear probes. *Front. Mar. Sci.* **11**, 1334327 (2024).
62. Bluteau, C. E. et al. Determining mixing rates from concurrent temperature and velocity measurements. *J. Atmos. Ocean. Technol.* **34**, 2283–2293 (2017).

Acknowledgements

We thank the crews of R/V Kay Kay-II, technicians from the Oceanographic Instrumentation Center (CIO, ANID grant CCSS210020), and students from the Department of Geophysics, University of Concepcion, who contributed to the field experiments. MP was supported by ANID Chile (Becas/Magister Nacional 2021/22211012). This research was supported by ANID/FONDECYT project N°1241203 and by the Millennium Institute of Oceanography (IMO, grants ICN12_019, AIM23-0003, and ICN2025_30). MP and BYQ are supported by the Swedish Formas Grant 2022-01536.

Author contributions

M.P. and O.P. contributed equally to the study design, field campaigns, and led the writing of the manuscript. M.P., O.P., A.R., L.P.V., O.U., P.F., M.R., and B.Y.Q. were involved in data analysis. All authors contributed to interpreting the results and writing the manuscript. L.P.V. and B.Y.Q. provided critical revisions and contributed to refining the final version of the manuscript.

Funding

Open access funding provided by University of Gothenburg.

Competing interests

The authors declare no competing interests.

Additional information

Supplementary information The online version contains supplementary material available at https://doi.org/10.1038/s43247-026-03194-8.

Correspondence and requests for materials should be addressed to Mauro Pinto-Juica or Oscar Pizarro.

Peer review information *Communications Earth and Environment* thanks the anonymous reviewers for their contribution to the peer review of this work. Primary handling editors: Sreelekha Jarugula and Alice Drinkwater. [A peer review file is available].